Article

Controlling CaCO$_3$ Particle Size with {Ca^{2+}}:{CO$_3^{2-}$} Ratios in Aqueous Environments

Sergěj Y. M. H. Seepma,* Sergio E. Ruiz-Hernandez, Gernot Nehrke, Karline Soetaert, Albert P. Philipse, Bonny W. M. Kuipers, and Mariette Wolthers

Cite This: *Cryst. Growth Des.* 2021, 21, 1576−1590

Read Online

ACCESS | Metrics & More | Article Recommendations | Supporting Information

ABSTRACT: The effect of stoichiometry on the new formation and subsequent growth of CaCO$_3$ was investigated over a large range of solution stoichiometries ($10^{-4} < r_{aq} < 10^4$, where r_{aq} = {Ca^{2+}}:{CO$_3^{2-}$}) at various, initially constant degrees of supersaturation ($30 < \Omega_{cal} < 200$, where Ω_{cal} = {Ca^{2+}}{CO$_3^{2-}$}/K_{sp}), pH of 10.5 ± 0.27, and ambient temperature and pressure. At r_{aq} = 1 and $\Omega_{cal} < 150$, dynamic light scattering (DLS) showed that ion adsorption onto nuclei (1−10 nm) was the dominant mechanism. At higher supersaturation levels, no continuum of particle sizes is observed with time, suggesting aggregation of prenucleation clusters into larger particles as the dominant growth mechanism. At $r_{aq} \neq 1$ (Ω_{cal} = 100), prenucleation particles remained smaller than 10 nm for up to 15 h. Cross-polarized light in optical light microscopy was used to measure the time needed for new particle formation and growth to at least 20 μm. This precipitation time depends strongly and asymmetrically on r_{aq}. Complementary molecular dynamics (MD) simulations confirm that r_{aq} affects CaCO$_3$ nanoparticle formation substantially. At r_{aq} = 1 and $\Omega_{cal} \gg 1000$, the largest nanoparticle in the system had a 21−68% larger gyration radius after 20 ns of simulation time than in nonstoichiometric systems. Our results imply that, besides Ω_{cal}, stoichiometry affects particle size, persistence, growth time, and ripening time toward micrometer-sized crystals. Our results may help us to improve the understanding, prediction, and formation of CaCO$_3$ in geological, industrial, and geo-engineering settings.
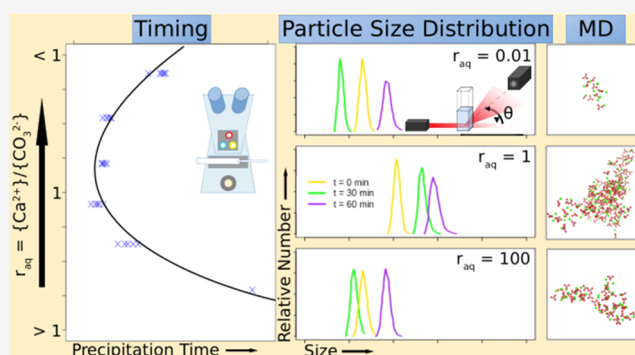
1. INTRODUCTION

CaCO$_3$ (lime)scale formation is a major problem in several practical fields, including drinking water distribution systems,[1] desalination of drinking water, appliances,[2,3] underground injection/extraction wells for usage of geothermal waters,[4] and oil industry.[5] In addition, precipitated CaCO$_3$ is used, for example, as a coating pigment in paper production.[6,7] Therefore, it is important to understand the influence of all partaking physicochemical parameters on the precipitation kinetics of CaCO$_3$, to impede undesirable limescale formation and/or tailor its precipitation.

Most natural waters are nonstoichiometric in relation to CaCO$_3$ since the {Ca^{2+}}:{CO$_3^{2-}$} ion activity ratio, r_{aq}, is affected by a range of parameters, including pH. For example, if we calculate the ion activity ratio for seawater containing an average chemical composition,[8] it shows an r_{aq} value of approximately 2.9×10^2, and this ratio will change due to ocean acidification, while for the water in Mono Lake, CL, it is about 5×10^{-4}.[9] Another example shows varying r_{aq} from about 1.74×10^2 to 1.7 before and after desalination of drinking water at the Weesperkarspel water treatment plant in Amsterdam.[10]

Ample research has focused on the influence of temperature, pressure, pH, ionic strength (I), specific background electrolytes, and supersaturation degree, especially with regard to calcite formation.[11−14] While research specifically focused on the impact of solution stoichiometry on calcite growth rate,[15−23] the timing of two-dimensional (2D) nucleation was not tabulated. Investigations also aimed at the new formation, or nucleation, of amorphous CaCO$_3$ (ACC),[24] ACC nucleation pathways,[25−36] inhibition by additives,[37−46] and the morphology of the nucleated crystals.[27] He et al.[47] and Stamatakis et al.[48] proposed an empirical equation to explain the nucleation time of calcite, based on their observations for stagnant and near-wellbore flow conditions, respectively. Notwithstanding, they assumed that the nucleation time depended only on temperature and supersaturation degree, disregarding pH, ionic strength, and other physicochemical

Table 1. Chemical Properties of the Investigated Growth Solutions[a]

solution nr.	HCl/NaOH	calculated parameters (MINTEQ)									measured parameters		type of performed experiment
		TOT·CaCl$_2$	TOT·Na$_2$CO$_3$	{Ca^{2+}}	TOT-CO$_3$	{CO$_3^{2-}$}	pH	I	Ω_{cal}	r_{aq}	pH[b]	{Ca^{2+}}[c]	
1.1	−0.68	0.8500	8.500	5.182×10^{-4}	3.790×10^{-3}	3.450×10^{-3}	11.01	0.195	50.2	0.155	10.82	n.d.	XPL
1.2	−0.92	2.461	2.461	1.915×10^{-3}	1.023×10^{-3}	9.291×10^{-4}	11.00	0.195	50.0	2.780	10.06	2.1×10^{-3}	XPL
1.3	−1.00	8.300	0.830	7.001×10^{-3}	2.793×10^{-4}	2.534×10^{-4}	10.99	0.195	49.9	29.171	10.61	n.d.	XPL
2.1	8.50	0.3600	360.0	3.115×10^{-5}	9.835×10^{-2}	8.973×10^{-2}	11.00	0.544	69.3	0.000342	11.10	n.d.	XPL
2.2	1.20	0.4900	49.00	1.177×10^{-4}	2.344×10^{-2}	2.133×10^{-2}	11.00	0.195	70.5	0.00672	10.45	4.0×10^{-4}	XPL
2.3	−0.60	1.026	10.26	5.883×10^{-4}	4.587×10^{-3}	4.175×10^{-3}	11.01	0.195	69.0	0.144	10.87	1.1×10^{-3}	XPL
2.4	−0.90	2.960	2.960	2.262×10^{-3}	1.212×10^{-3}	1.100×10^{-3}	10.99	0.195	70.0	2.179	10.64	2.9×10^{-3}	XPL and DLS
2.5	−1.00	10.20	1.020	8.570×10^{-3}	3.244×10^{-4}	2.944×10^{-4}	10.99	0.194	71.0	31.499	10.47	1.1×10^{-2}	XPL
2.6	−1.15	45.50	0.4550	4.016×10^{-2}	6.795×10^{-5}	6.173×10^{-5}	11.00	0.195	69.8	679.700	10.35	n.d.	XPL
3.1	9.20	0.4300	430.0	3.432×10^{-5}	1.027×10^{-1}	9.354×10^{-2}	11.00	0.621	84.9	0.000361	11.12	n.d.	XPL
3.2	1.60	0.5650	56.50	1.212×10^{-4}	2.732×10^{-2}	2.484×10^{-2}	11.00	0.195	84.7	0.00485	11.03	n.d.	XPL
3.3	−0.55	1.163	11.63	6.384×10^{-4}	5.190×10^{-3}	4.725×10^{-3}	11.01	0.195	84.9	0.138	10.86	n.d.	XPL
3.4	−0.90	3.295	3.295	2.488×10^{-3}	1.335×10^{-3}	1.214×10^{-3}	11.00	0.195	84.8	2.147	10.70	n.d.	XPL
3.5	−1.00	11.38	1.138	1.061×10^{-2}	3.763×10^{-4}	3.414×10^{-4}	10.99	0.195	85.1	31.616	10.59	n.d.	XPL
3.6	−1.17	53.00	0.5300	5.333×10^{-2}	7.349×10^{-5}	6.678×10^{-5}	10.99	0.196	85.1	748.358	10.57	n.d.	XPL
4.1	10.00	0.4900	490.0	3.666×10^{-5}	1.050×10^{-1}	9.531×10^{-2}	10.99	0.685	98.6	0.000130	11.11	5.0×10^{-4}	XPL
4.2	2.00	0.6400	64.00	1.241×10^{-4}	3.122×10^{-2}	2.836×10^{-2}	11.00	0.195	98.9	0.00434	11.04	6.0×10^{-4}	XPL and DLS
4.3	−0.50	1.275	12.75	6.780×10^{-4}	5.381×10^{-3}	4.877×10^{-3}	11.01	0.194	98.4	0.122	10.86	1.1×10^{-3}	XPL
4.4	−0.90	3.610	3.610	2.696×10^{-3}	1.449×10^{-3}	1.318×10^{-3}	11.00	0.195	100.0	2.320	10.41	2.9×10^{-3}	XPL and DLS
4.5	−1.00	12.69	1.269	1.061×10^{-2}	3.763×10^{-4}	3.414×10^{-4}	10.99	0.196	101.6	32.629	10.60	9.5×10^{-3}	XPL
4.6	−1.20	60.00	0.6000	5.333×10^{-2}	7.349×10^{-5}	6.678×10^{-5}	11.00	0.195	100.2	833.333	10.43	5.5×10^{-2}	XPL and DLS
5.1	12.00	0.699	699.0	4.260×10^{-5}	1.056×10^{-1}	9.471×10^{-2}	10.98	0.893	150.0	0.000445	11.08	n.d.	XPL
5.2	2.00	0.9000	90.00	1.276×10^{-4}	4.584×10^{-2}	4.171×10^{-2}	11.00	0.195	149.6	0.00301	11.08	9.0×10^{-4}	XPL
5.3	−0.35	1.665	16.65	7.920×10^{-4}	7.380×10^{-3}	6.722×10^{-3}	11.01	0.195	149.6	0.120	10.89	1.5×10^{-3}	XPL
5.4	−0.85	4.550	4.550	3.296×10^{-3}	1.779×10^{-3}	1.616×10^{-3}	11.00	0.196	149.6	2.162	10.64	4.1×10^{-3}	XPL and DLS
5.5	−1.05	16.10	1.610	1.340×10^{-2}	4.364×10^{-4}	3.974×10^{-4}	11.01	0.1944	150.0	35.789	10.53	1.3×10^{-2}	XPL
5.6	−1.30	85.00	0.8500	7.496×10^{-2}	8.451×10^{-5}	7.702×10^{-5}	11.00	0.2352	150.3	1023.350	10.31	7.4×10^{-2}	XPL
5.7	−2.90	618.0	0.618	2.980×10^{-1}	8.943×10^{-6}	7.864×10^{-6}	11.00	1.2153	150.0	38 338.745	10.59	n.d.	XPL
6.1	4.50	1.165	116.5	1.459×10^{-4}	5.660×10^{-2}	5.139×10^{-2}	10.98	0.2224	199.5	0.00280	11.06	1.2×10^{-3}	XPL
6.2	−0.20	2.010	20.10	8.750×10^{-4}	8.898×10^{-3}	8.102×10^{-3}	11.01	0.1945	199.5	0.110	10.88	1.8×10^{-3}	XPL
6.3	−0.80	5.370	5.370	3.793×10^{-3}	2.062×10^{-3}	1.869×10^{-3}	11.00	0.1945	199.5	2.128	10.69	4.3×10^{-3}	XPL and DLS
6.4	−1.05	20.00	2.000	1.657×10^{-2}	4.944×10^{-4}	4.501×10^{-4}	11.00	0.1949	200.9	39.099	10.51	1.7×10^{-2}	XPL
6.5	−1.40	110.0	1.100	9.461×10^{-2}	9.570×10^{-5}	8.745×10^{-5}	11.00	0.3001	200.0	1105.831	10.57	n.d.	XPL

[a]Concentration units are displayed in mol L^{-1}; negative numbers in the second column indicate NaOH, and positive numbers indicate HCl; n.d. stands for not determined; XPL indicates cross-polarized light in optical light microscopy; DLS represents dynamic light scattering. [b]pH was measured within seconds after mixing. [c]{Ca^{2+}} was measured in the growth solution prior to mixing.

parameters. Nevertheless, to the best of the authors' knowledge, no systematic study on the impact of solution $\{Ca^{2+}\}$:$\{CO_3^{2-}\}$ ion activity ratio at a constant degree of supersaturation on $CaCO_3$ nucleation has been carried out.

In this work, we combined the use of in situ dynamic light scattering (DLS) and polarized light microscopy (PLM) techniques with molecular simulations to investigate the effect of solution stoichiometry on the new formation (nucleation) and subsequent growth of $CaCO_3$ over a large range of supersaturation. Furthermore, we used statistical analysis to derive a new empirical relationship that links precipitation time, i.e., the time needed for new particles to nucleate and grow to crystals of at least 20 μm, to I, r_{aq}, pH, and Ω_{cal}.

2. MATERIALS AND METHODS

2.1. Preparation of Growth Solutions. Visual MINTEQ—a free equilibrium speciation model[49]—version 3.1 was used to calculate target Ω_{cal}, r_{aq}, pH, and I for a set of growth solutions, where Ω_{cal} is defined as

$$\Omega_{cal} = \frac{\{Ca^{2+}\}\{CO_3^{2-}\}}{K_{sp}} \tag{1}$$

where K_{sp} is the solubility product of calcite ($10^{-8.48}$ at 25 °C).[50] Growth solutions were prepared by dissolving reagent-grade salts into ultrapure water (UPW) (ISO 3696 standard grade, 1−18 mΩ); separate solutions of Na_2CO_3 (Sigma-Aldrich) and $CaCl_2$ (Sigma-Aldrich) were prepared. The solution pH and ionic strength were adjusted by the addition of NaOH, HCl, and NaCl (Sigma-Aldrich). The ionic strength of the desired growth solutions for these experiments was 0.19−0.20 M, to ensure that I remained constant during precipitation.

All calculations within Visual MINTEQ were done using the Davies equation[51] at a temperature of 20 °C assuming a system closed to the atmosphere, i.e., comparable to our experimental conditions. The aimed pH of the solution was 11. Table 1 lists all of the used growth solutions with their physicochemical parameter values.

The $CaCl_2$−NaCl−NaOH/HCl and Na_2CO_3 solutions used for the different experiments were prepared from the following set of previously prepared stock solutions: 0.05 and 1 M Na_2CO_3; 1 mM and 1 M $CaCl_2$; 1 M NaCl, 1 M NaOH, and 1 M HCl. The Na_2CO_3 stock solutions were kept in a sealed bag (originally optimized for gas sampling applications) to minimize possible CO_2 exchange with the atmosphere. Growth solutions of 150 mL were prepared from the stock solutions and kept in stoppered glass beakers until experiments were performed (always within 48 h).

The pH and $\{Ca^{2+}\}$ of our combined starting solutions were measured to monitor the initial experimental conditions (i.e., it allowed comparison with the calculated physicochemical conditions). The pH was measured by a pH meter (type: WTW Multi 340i with a WTW SENTIX HWD pH electrode), while $\{Ca^{2+}\}$ was measured using an ion-selective electrode (ISE) (Thermo Fisher; type: 9720BNWP) attached to an Orion Visastar 40B Benchtop Multimeter.

2.2. Particle Size Measurements. The nucleation and growth of $CaCO_3$ were investigated using dynamic light scattering (DLS) with a Zetasizer Nano ZS[52] equipped with Zetasizer Software v7.10.[53] The laser wavelength and laser power used were 633 nm and 4 mW, respectively. Experiments were conducted along with noninvasive backscattering detection (NIBS), because $CaCO_3$ causes multiple scattering due to its high contrast in the refractive index (RI).[54] Using NIBS, the multiple scattering effect was reduced[55,56] and the scattering information was obtained at 173°. If the particle can be considered to be spherical, the Rayleigh scattering intensity is related to the sixth power of the hydrodynamic radius of the particle (I_R α R_H^6)[57] and that same hydrodynamic radius is related to the translational diffusion coefficient via the Stokes−Einstein relationship[53,58,59]

$$D_{Trans} = \frac{k_b T}{6\mu\pi R_H} \tag{2}$$

where k_b is the Boltzmann constant (m^2 kg s^{-2} K^{-1}), T is the absolute temperature (K), μ is the dynamic viscosity (kg s^{-1} m^{-1}), R_H is the hydrodynamic diameter (m), and D_{Trans} is the translational diffusion coefficient (m^2 s^{-1}).

The DLS measurements were taken using (10 × 10 mm^2) disposable polystyrene cuvettes, which were cleansed beforehand with UPW water and dried. Both the calcium and carbonate solutions were squeezed through 0.2 μm disposable nylon syringe filters before mixing, to remove as much dust particles as possible. Thereafter, the solutions were poured into the cuvette and, upon mixing, the cuvette was quickly closed and inserted in the Zetasizer Nano ZS. During this process, we have taken the utmost care to avoid artificial density variations due to the presence of dust particles (filtration of growth solutions) and air bubbles (careful filling of cuvettes and visual checks for air bubbles). Note though, in the systems under investigation, it is highly unlikely that bubbles will form during ongoing reactions. Measurements were conducted at a temperature of 20 ± 0.1 °C for a set of growth solutions (Table 1). The particle size results were obtained using the non-negative least squares as the discrete inversion approach.[60] We used the CONTIN approach as a regularization method.[61,62] The error of the measured particle size in the cuvette may be as large as 10% for a particle size of ~1000 nm.[63,64]

To compare the DLS results with the ones of the MD simulations, we converted the particle size into the number of growth units a particle of certain size contains by assuming that the size of a $CaCO_3$ unit is 0.3 nm[65,66] and that the constituent ions of the particle were spheres packed in the most dense way (i.e., a random close packing (RCP) value of 74.04%).

2.3. Nucleation Plus Growth Time Measurements. The setup for the PLM measurements using cross-polarizers (XPL) is depicted in Figure S1 in Section SI in the Supporting Information (SI). To maintain pressure on the tubing during flow, a peristaltic pump (Ismatec IPC-N-08; SKU: ISM936D) equipped with Click-n-go POM-C cassettes was used. Tygon Long Flex Life tubing (two-stop color-coded tubing; Ismatec reference: SC0424), with an inner diameter of 1.52 mm and a wall thickness of 0.86 mm, was used. Two tubes were placed in their cassettes onto the peristaltic pump. To minimize the potential pressure differences between both cassettes, they were placed directly next to each other. The tubing was cut, so they had the same length between the points where they took up the growth solutions and the connection point where both growth solutions came together. The connection point consisted of a small nylon Y-shaped connector. Behind the connection point, both growth solutions flowed into a soda lime glass pasteur pipet (14.6 cm length, 0.65 cm in diameter; Corning 7095B-X5), which was placed under XPL (see Figure S1 in Section SI in the SI).

In XPL, crystalline material will only become visible from a threshold size that depends on the refractive index. For calcite, this is from ~20 μm (explained in Section SII, SI). Whenever two crystals were visible under XPL (Figure S3 in Section SIII, SI), this was defined as the precipitation time. Therefore, the precipitation time is the time needed for nucleation plus growth of the calcite crystals to a size of approximately 20 μm. Since this time includes a stochastic process,[67−69] at least five duplicate runs were performed. The following steps were performed before each run to ensure identical starting conditions: (i) Flushing for 30 s with deionized water; (ii) flushing for 15 s with 10% HCl; (iii) flushing for 15 s with deionized water to drive HCl out again; (iv) drying the tubes and Pasteur pipette before filling them with growth solution again; (v) flushing until the precipitating solution, i.e., the solution containing both Ca^{2+} and CO_3^{2-}, reached about 2 cm in the thicker part of the glass pipet; (vi) stop flow; and (vii) start precipitation time measurement.

2.4. Molecular Dynamics Simulations. MD simulations were preformed to further investigate the ionic interactions influencing nanoparticle formation and properties. However, simulations under similar experimental conditions (Table 1) require huge systems, resulting in exorbitant computational costs. Therefore, $\Omega_{cal} \gg 1000$
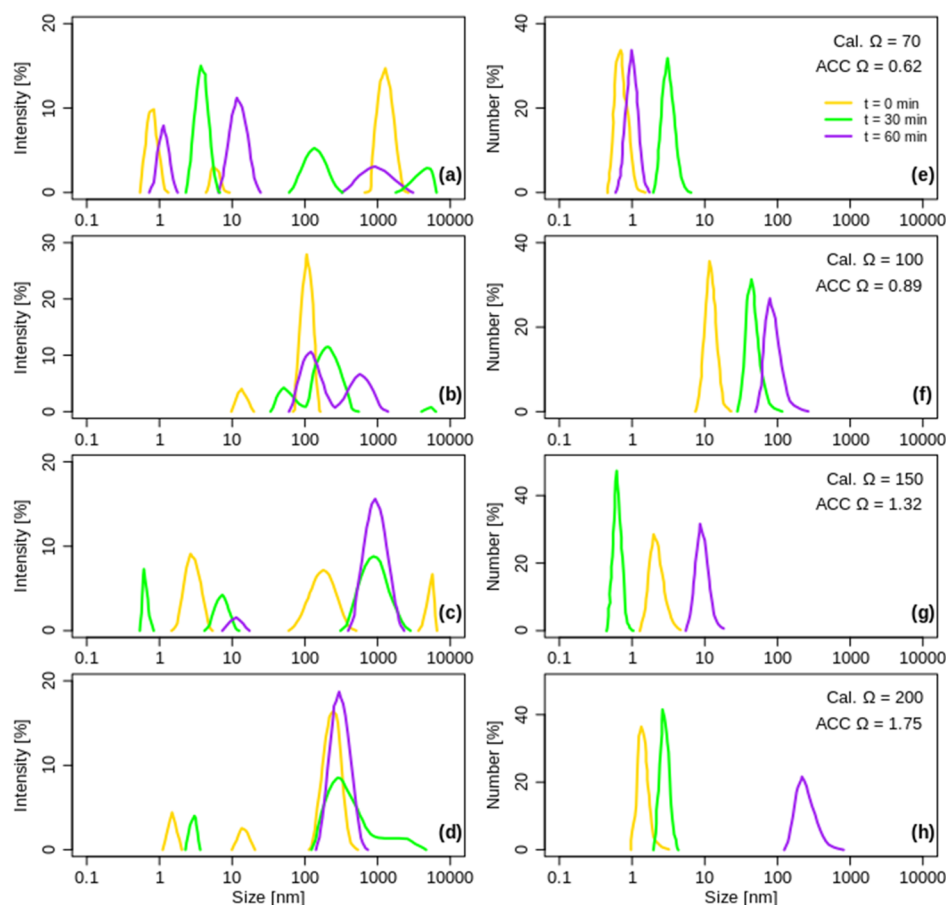
Figure 1. Relative intensity of scattered light (%) versus particle size (nm) (a–d) and the relative amount of particles (number) (%) plotted against the size of particles (nm) (e–h), under near-stoichiometric conditions and different Ω values for the first hour of the precipitation reaction. Ω_{cal} increases from top to bottom from 70 to 200. In all cases, the yellow color represents a rough initial measurement, the green color after approximately half an hour, and the purple color represents a measurement after 1 h.

was chosen for the simulations performed both by previous workers and in the current study, to facilitate prenucleation particle formation within achievable simulation times without biasing the simulations. In addition, our selected number of atoms in the system (which defines the value of Ω_{cal}) was targeted to fall in between the amount that Demichelis et al.[28] and Smeets et al.[31] used.

Two opposite sets of systems were created to support our experimental findings: (i) single large ACC particles in a liquid water−molecule/ion mixture that represents the experimental solutions after precipitation and (ii) liquid water−molecule/ion mixtures that represent the experimental solutions before precipitation.

For the first set of systems, a random stoichiometric ACC particle of 255 formula units was generated (following the method of Raiteri and Gale[70]), with a radius of gyration of ∼1.4 nm (e.g., a similar size to the observed prenucleation cluster; see Section 3.3) that was then surrounded by 15 813 water molecules in a cubic simulation cell of 78.19 Å. From that initial cluster, a range of cations or anions (maximum of 17) from the most external layers were removed to recreate nonstoichiometric particles of $CaCO_3$. The same r_{aq} of the most external layers of the particle was also kept in solution, by placing a number of both Ca^{2+} and CO_3^{2-} fully dissolved. The electroneutrality of the simulation cell was achieved using counterions of Na^+ or Cl^-, similar to the experiments.

For the second set of systems, the total amount of ions were placed fully dissolved in the same simulation box. We simulated a stoichiometric system and two nonstoichiometric systems with Na^+ and Cl^- counterions for electroneutrality. Using this system setup, the formation of $CaCO_3$ could be simulated in close comparison to the DLS experiments. The evolution of time of both groups of systems

was followed by classical molecular dynamics simulations to see if and how the different systems dissolved or precipitated in time.

The $CaCO_3$−water systems were simulated using the force field of Demichelis et al.,[28] with the Cl^-−water interaction from Spagnoli et al.[71] The MD runs were performed in the *NPT* ensemble at 300 K using the DL_POLY code (version 4.09), where all atoms were allowed to move during the simulations with a timestep of 1 fs. A Nosé−Hoover thermostat and barostat was used with 0.1 and 1 ps relaxation times. The total simulation time was 20 ns, including the initial 100 ps until equilibration. The convergence of the results with respect to all of the precision parameters and the stability of the system evolution during the equilibrium phase were carefully tested.

We calculated the normalized energy of the system according to the following equation

$$E_{nor} = \frac{E_{conf}}{E_{solv}} \tag{3}$$

where E_{conf} is the averaged configurational energy obtained over the last 100 ps of production and E_{solv} is the energy of a system with the same number of atoms, but when all of the ions are fully dissolved.

2.5. Statistical Analysis. R-software[72] was used to derive a new empirical relationship to describe precipitation time in terms of Ω_{cal}, r_{aq}, pH, and *I*, based on our XPL experimental observations. A full description of the derivation is given in Section SIV, SI. In summary, the nonlinear least-squares (nls) method was used to find the relationship, and subsequently, Bayesian analysis was performed to optimize that relationship. The suite required the use of the "FME" package, associated with the "FMEother" and "FMEmcmc" vignettes.[73] Fitting of the nonlinear model was carried out according

to the procedure described in the "FMEother" vignette, while the "FMEmcmc" vignette was followed to run the Markov chain Monte Carlo (MCMC) Bayesian analysis. The MCMC analysis was carried out using the Adaptive Metropolis (AM) with Delayed-Rejection (DR) algorithm;[74] upon rejection, the next parameter candidate is tried [ntrydr = 3]. This was done to overcome the drawback of having an increasing target density, going to one.[75]

3. RESULTS AND DISCUSSION

3.1. Growth Solutions' Composition. To ascertain if the physicochemical parameters calculated using Visual MINTEQ matched with the actual growth solutions, the measured pH and free Ca^{2+} activity are listed in Table 1. They are in good agreement with the calculated pH and free Ca^{2+} activity. Overall, the measured pH is somewhat lower than the calculated pH and reveals a distribution of 10.5 ± 0.27, rather than pH 11. This may largely be attributed to the measurement delay (several seconds) directly upon mixing. Remarkably, the pH was predominantly lower than expected in lower TOT-CO_3 mixtures, which have a stronger sensitivity to pH changes.[76−78] Reequilibration of the carbonate species upon mixing of the $CaCl_2-NaCl-NaOH/HCl$ and Na_2CO_3 solutions, due to deprotonation of HCO_3^- and formation of $CaCO_3$ phases, likely lowered the pH somewhat during that period.

3.2. $CaCO_3$ Particle Size Evolution with Time at r_{aq} = 1. A critical note should first be made with respect to the suggested differentiation of particles of certain size. Since one $CaCO_3$ unit is about 0.3 nm[65,66] and its hydrodynamic radius somewhat larger (Debye length ∼ 0.7 nm at I = 0.2 M), it was assumed that the lowest detectable size limit for a $CaCO_3$ unit was about 1 nm and that growth units forming a larger particle, whose size is up to approximately 100 nm, cannot form a definite crystal structure yet under relatively low to moderate Ω_{cal}. For that reason, we refer to prenucleation particles (in which we distinguish between nuclei, referring to ion-by-ion growth, and prenucleation clusters, referring to the nonclassical nucleation pathway involving prenucleation clusters[31]) if the measured particle size is <100 nm. As was pointed out by De Yoreo and Vekilov,[79] the size range in which nanoparticles can be regarded as a prenucleation particle, i.e., smaller than the critical nucleus size, depends among others on the chemical conditions (mainly Ω) and varies typically in the range of about 1−100 nm. However, note that nanoparticles smaller than 100 nm have been reported to be crystalline (e.g., for iron sulfides, Wolthers et al.[80] and Michel et al.,[81] and for iron oxides, Gilbert et al.[82]). Reportedly, the smallest crystalline $CaCO_3$ particles, observed with transmission electron microscopy, are about 10 nm.[83]

In our dynamic light scattering data, we therefore distinguish three measured particle size ranges: ±1−100 nm, referred to here as prenucleation particles; ∼100 to 2000 nm, assumed to represent precipitated material; and >2000 nm, may represent dust particles, despite filtration. However, our XPL experiments indicated that calcite crystals of size >20 μm can form within 15 min in Ω_{cal} = 70 to within less than 2 min in Ω_{cal} = 200. Therefore, most of the >2000 nm peaks likely represent larger $CaCO_3$ particles. Note that particles >10 μm are outside of the (quantifiable) size range for DLS.

We compared the $CaCO_3$ crystal formation at different Ω_{cal} values, while keeping the initial r_{aq} constant, looking at the particle size distribution based on the scatter intensities (Figure 1a−d) and the number of particles (Figure 1e−h).

As a first approximation, the model of an equivalent homogeneous sphere is applied. The yellow curves show the particle size distribution observed at t = 0, but in practice, it is 20−30 s after the onset of the precipitation reaction due to initialization/calibration of the Zetasizer. Under stoichiometric conditions at Ω_{cal} = 70, a large number of prenucleation-sized particles were observed (Figure 1a,e), while some particles larger than 10 nm were also observed (Figure 1a). Yet, the latter were not visible when plotting the number of particles instead of scattering intensity (Figure 1e) because the difference in measured particle size is about 1−2 orders of magnitude, resulting in a difference in the number of particles as large as 6−12 orders in magnitude according to eq 2. The apparent particle size appeared to fluctuate over the first hour, and it remained below 10 nm over the course of 3 h (Figure S6a,e in Section SVI, SI). In contrast, at Ω_{cal} = 100, the dominant apparent particle size was within the size range of 10−200 nm (Figure 1b,f) and showed a steady increase over the first 3 h up to ± 300 nm (Figure S6b,f in Section SVI, SI). The peak occurring at <1 nm after 3 h is most likely related to ion-pair formation in combination with settling of larger particles. Similar to Ω_{cal} = 70, both prenucleation-sized and precipitate-sized particles were detectable at Ω_{cal} = 150 for the first hour (Figure 1c,g), and the apparent size also fluctuated with time. However, contrary to Ω_{cal} = 70, the intensities for the latter group of apparent particle sizes are larger compared to the intensities contribution shown for particles of 1−10 nm and became more pronounced over the course of 3 h (Figure S6c,g in Section SVI, SI). Nonetheless, due to the I_R-R_H relationship (Rayleigh scattering), the peaks are not visible in the number versus size plot. At Ω_{cal} = 200, however, the difference in relative intensity between these two population distributions was larger compared to Ω_{cal} = 150 and, therefore, a peak at precipitate-sized particles (∼220 nm) was observed after 1 h (Figure 1d,h). These peak heights do not persist over the course of 3 h, as the difference in intensities for the two population distributions was not maintained as large (Figure S6d,h in Section SVI, SI), most likely due to settling of these particles through time.

In this series of experiments, we cross the equilibrium with amorphous calcium carbonate (ACC). Our experiments at Ω_{cal} < 100 are still most likely undersaturated with respect to ACC ($K_{sp,ACC}$ = $10^{-6.40}$ according to Brečević and Nielsen,[84] although there is still some debate about the solubility of ACC[85−87] and other K_{sp} values for ACC of $10^{-6.04}$, $10^{-7.51}$, and $10^{-7.70}$ have been suggested by, respectively, Clarkson et al.,[88] Gebauer et al.,[25] and Lassin et al.[89]). Nonetheless, this would mean that in our experiments, $CaCO_3$ formation occurs most likely via an ACC precursor, at Ω_{cal} > 100. Similar to Steefel and Van Cappellen,[90] we therefore assume that homogeneous (three-dimensional (3D)) nucleation occurs above the operationally defined threshold of Ω_{cal} > 100.

At Ω_{cal} = 70, the predominance of prenucleation-sized particles (Figure 1e) suggests that the transition to precipitated material did not happen within an hour. Alternatively, such a low number of precipitate-sized particles was formed that it cannot be quantified with the DLS (Figure 1a versus e). Moreover, no clear trend can be observed in the evolution of apparent particle size (Figure 1e). Contrastingly, at Ω_{cal} = 100, the evolution of more dominant measured particle size range of 10−100 nm (Figure 1f) may imply that the precipitation process at this supersaturation degree has preferentially proceeded via ion-by-ion adsorption,[91,92] as the gradual
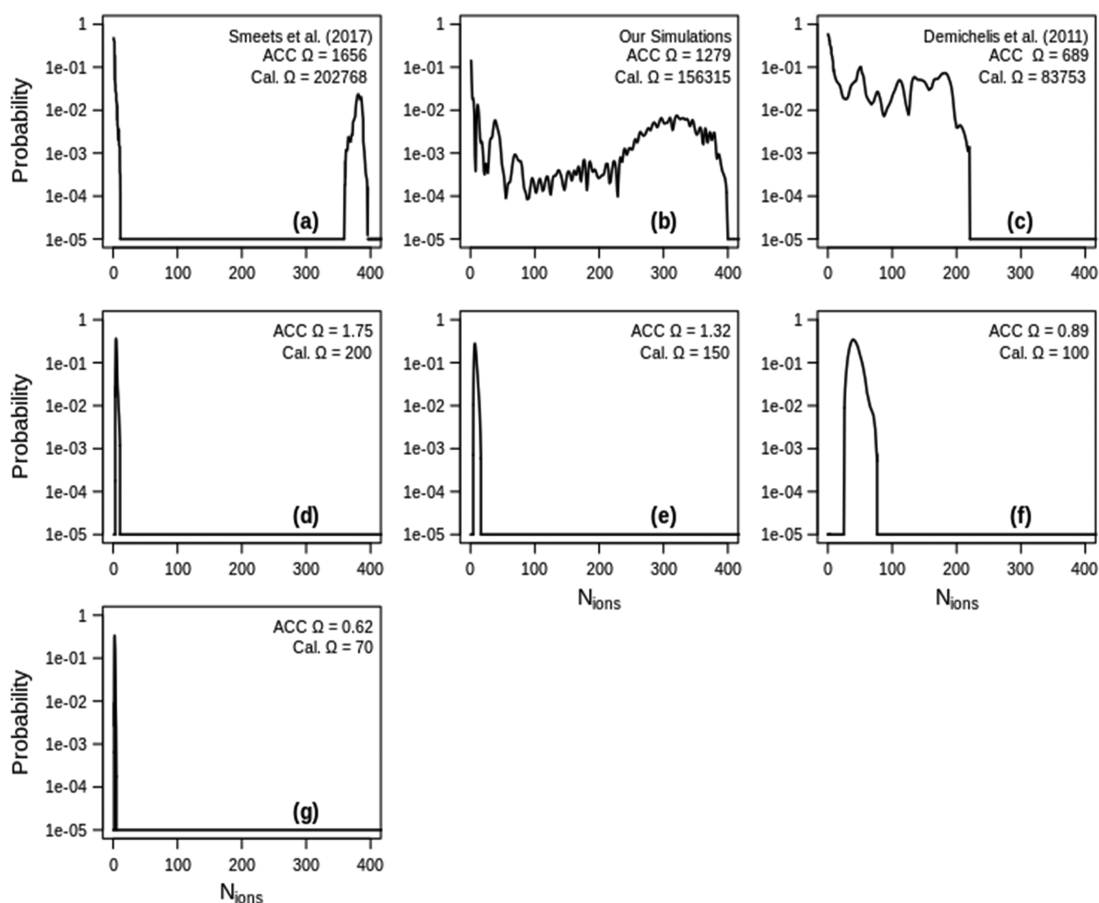
Figure 2. Probability (log-scale) of an aggregate of certain size (consisting of a number of ions) at different omega values. Both the omega values for calcite and ACC are given. The images (a−c) are based on MD simulations, while (d−g) are based on experimental DLS results. ACC is the only polymorph created in the MD simulations, while during the experiments, it can be ACC, vaterite, and/or calcite (for $\Omega > 100$) or vaterite and/or calcite (for $\Omega \leq 100$). The solubility for ACC is based on the solubility product, $10^{-6.40}$, found by Brečević and Nielsen.[84]

increase of measured particle size with time could indicate this. This potential indicator becomes more distinct over much longer time ranges (about 15 h) and depends greatly on Ω_{cal} (Figure S7 in Section SVII, SI). At $\Omega_{cal} = 100$, the precipitates slowly and continuously increase in apparent particle size, which may suggest ion-by-ion growth. If only peaks significantly larger than 100 nm would exist besides peaks at prenucleation particle sizes, the precipitation of $CaCO_3$ may proceed preferentially via aggregation rather than ion-by-ion adsorption. Such separate populations of peaks were observed at $\Omega_{cal} = 150$ (Figures 1c,g and S7b), where precipitate-sized particles were present in the sample and no continuum of increasing particle size distributions with time was observed. If the presence of peaks ≫100 nm is indicative of aggregation of prenucleation clusters, then this was the preferential process at $\Omega_{cal} = 150$ for nucleation and crystal growth. At $\Omega_{cal} = 200$ (Figures 1d,h and S7c), an even higher percentage in precipitate-sized particles was observed, with sizes in the order of 200−400 nm, which suggests a higher degree of crystal nucleation via prenucleation cluster aggregation and subsequent growth.

The preferential aggregation pathway that we observed at $\Omega_{cal} > 100$, likely encompasses the onset of nucleation via stable prenucleation clusters, which may be involved with aggregation into an ACC phase, by colliding and coalescing, and final transformation to a crystal phase.[25,93] The latter was also found by Wang et al.,[24] who showed that the effect of

initial ACC formation becomes apparent at $\Omega_{cal} > 100$, based on their turbidity experiments. Usually, ACC is much smaller in size compared to crystalline material and presents itself often in different sizes.[94] This may explain the over-representation of peaks in the range of 50−200 nm at $\Omega_{cal} > 100$ (Figure S7 in Section SVII, SI). This size range roughly coincides with the work of Nielsen et al.,[95] who studied (in situ) direct formation of ACC under neutral pH conditions and concordant Ω_{cal} conditions. ACC particles grew to approximately 500 nm in about 90 s, and after 5 min, some particles reached a size as large as 1 μm. At approximately that size, ACC began to shrink just before transformation into a subsequent crystalline phase.[95] We observed (Figure 1), similar to Nielsen et al.,[95] on several occasions particle size reduction with time, which may suggest a similar process of transformation from ACC to a more crystalline phase.

The experimental results (Figure 1) can be compared with the MD simulations, when all results are translated into a probability versus the number of ions (Figure 2). Note that this comparison extends over a wide range of Ω, with the highest Ω results obtained using MD simulations. The simulations inform us on the impact of solution (non)-stoichiometry on particle formation and stability. Since the only known main switch in particle formation mechanism occurs at $\Omega_{cal} = 100$ (to the best of our knowledge), we assume that, what we observed in the simulations is likely valid for our experiments at $\Omega_{cal} > 100$.
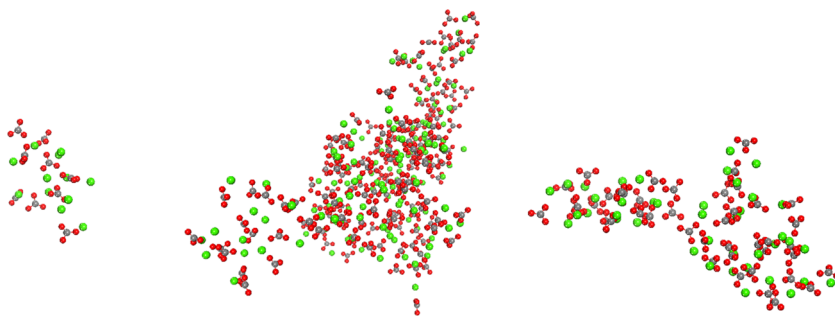
Figure 3. Size (gyration radius) of the largest particle present in the system after 20 ns, for three stoichiometrically different systems starting with fully solvated ions. The gyration radii for the particle after 20 ns for the system starting with $r_{aq} = 0.77$ are 0.6 nm (left), 1.9 nm for $r_{aq} = 1.00$ (middle), and 1.5 nm for $r_{aq} = 1.30$ (right).

For these systems, the maximum particle size that the simulation cell can contain, based on the amount of ions that were put in the cell, lies around 400 $CaCO_3$ units for Figure 2a, 500 for Figure 2b, and most likely about 250 for Figure 2c (although Demichelis et al.[28] did not mention the exact number of ions used in the simulation cell). The limited amount of ions in all cases was due to system size limitations. All MD simulations (Figure 2a–c) initially had all ions dissolved, and cluster formation was observed within 20 ns. At the highest Ω value (Figure 2a; MD data from Smeets et al.[31]), the two distinct peaks represent particles that contain about 400 ions and very small particles/ion pairs, which may imply the addition of ion pairs/small particles to a single large particle. It was previously implied that the ion pairs/small particles (three to five ions) are indicative of the formation of a dense liquid phase that grows into the large particle.[31,96]

In our simulations under stoichiometric conditions and somewhat lower Ω values (Figure 2b), we observed a broad probability distribution in particle size. It is noteworthy that two peaks began to form in the broad probability distribution, one at ion pairs/small particles size and one that exceeds an amount of 300 ions. Most likely, with further increase in the simulation time, the result would have been two main peaks, following the trend of Smeets et al.[31] At even lower Ω values (Figure 2c; MD data from Demichelis et al.[28]), only one broad peak is observed after 20 ns of simulation time, indicating a wide range of particle sizes. It is unclear from this simulation at prolonged simulation time, if a similar trend would evolve (as for the higher Ω MD simulations) or if a broad size distribution would remain.

The trends observed in the MD simulations are continued in the probabilities obtained from the $t = 0$ min DLS measurements (Figure 2d–g). At $\Omega_{cal} = 200$ and 150, only large peaks of ion pairs/small particles occurred, indicating that time was too limited for the systems to evolve to a wider size distribution. Decreasing Ω_{cal} further to 100 resulted in undersaturation with respect to ACC, and the peak observed at $t = 0$ min became broader and shifted toward slightly larger particles, likely due to increasing contribution of calcite crystal growth versus prenucleation cluster formation and aggregation. However, at $\Omega_{cal} = 70$, time was again too limited for the system to show any growth of particles.

To summarize, going from highest to lowest degree of supersaturation with respect to ACC, we observed that the development of (a) large particle(s) in a solution with ion pairs/small particles takes increasingly more time (Figure 2a–c) until only small ion pairs/small particles remain (Figure 2d,e). When the solution becomes undersaturated with respect

to ACC (Figure 2f,g), this trend is repeated, with the broader distribution of measured particle sizes becoming narrower toward the lowest Ω_{cal}.

3.3. CaCO$_3$ Particle Size Evolution with Time at $r_{aq} \neq 1$. Besides the influence of Ω, the impact of stoichiometry on the process of nucleation and growth was assessed for different stoichiometries at initial $\Omega_{cal} = 100$ using DLS and $\Omega_{cal} \approx 156\,000$ using MD simulations. The relative intensity and number of particles observed using DLS at $r_{aq} \sim 0.01$, ~ 1, and ~ 100 are found in Figure S8 in Section SVIII, SI. The measurements at $t = 0$ min showed much smaller particle sizes under nonstoichiometric conditions than at $r_{aq} \sim 1$, and there seemed to be more fluctuations of particle size with time; after 30 min, the measured particle size was smaller than at $t = 0$ min, and after 60 min, the apparent particle size had increased a little again, but always remained below 10 nm. There was no significant difference in relative intensity or measured particle size between the sample with $r_{aq} \sim 0.01$ and ~ 100. Contrastingly, at $r_{aq} \sim 1$, the measured particle size increased consistently with time to about 100 nm over the first hour. Over longer timescales (Figure S9 in Section SIX, SI), generally, the same trends were observed, with the notable exception of the measurement at $t = 180$ min at $r_{aq} \sim 1$. Under nonstoichiometric conditions, the apparent particle size remained below 10 nm, while at $r_{aq} \sim 1$, the measured particle size increased. In the final DLS measurement at $r_{aq} \sim 1$, we observe a (few) particle(s) of approximately 500 nm and new appearance of ion pairs/small particles of ~ 1 nm. Potentially, this latter trend is either caused by continued ion-pair formation of the constituent ions in the solution combined with the increase in sedimentation of larger particles or reflects an Oswald ripening process similar to that observed by Nielsen et al.[97] using liquid-cell transmission electron microscopy, where ACC rapidly dissolved during the formation of slightly smaller calcite crystals. The formation of larger-sized particles at $r_{aq} \sim 1$ than under nonstoichiometric conditions was also observed in our MD simulations (Figure 3). In addition, larger particles are present in the system where Ca^{2+} is more abundant ($r_{aq} = 1.30$) compared to the system where CO_3^{2-} is more abundant ($r_{aq} = 0.77$).

To confirm that the particles formed in these simulations are more stable than the dissolved ions of the initial MD configuration, we used eq 3 to calculate the normalized energy of the simulated systems, as an indication of its thermodynamic stability (Figure S10 in Section SX, SI). If the normalized energy is larger than 1, then the particles, ion pairs, and small particles are more stable than fully solvated ions. Figure S10a shows the normalized energy for the systems starting with one
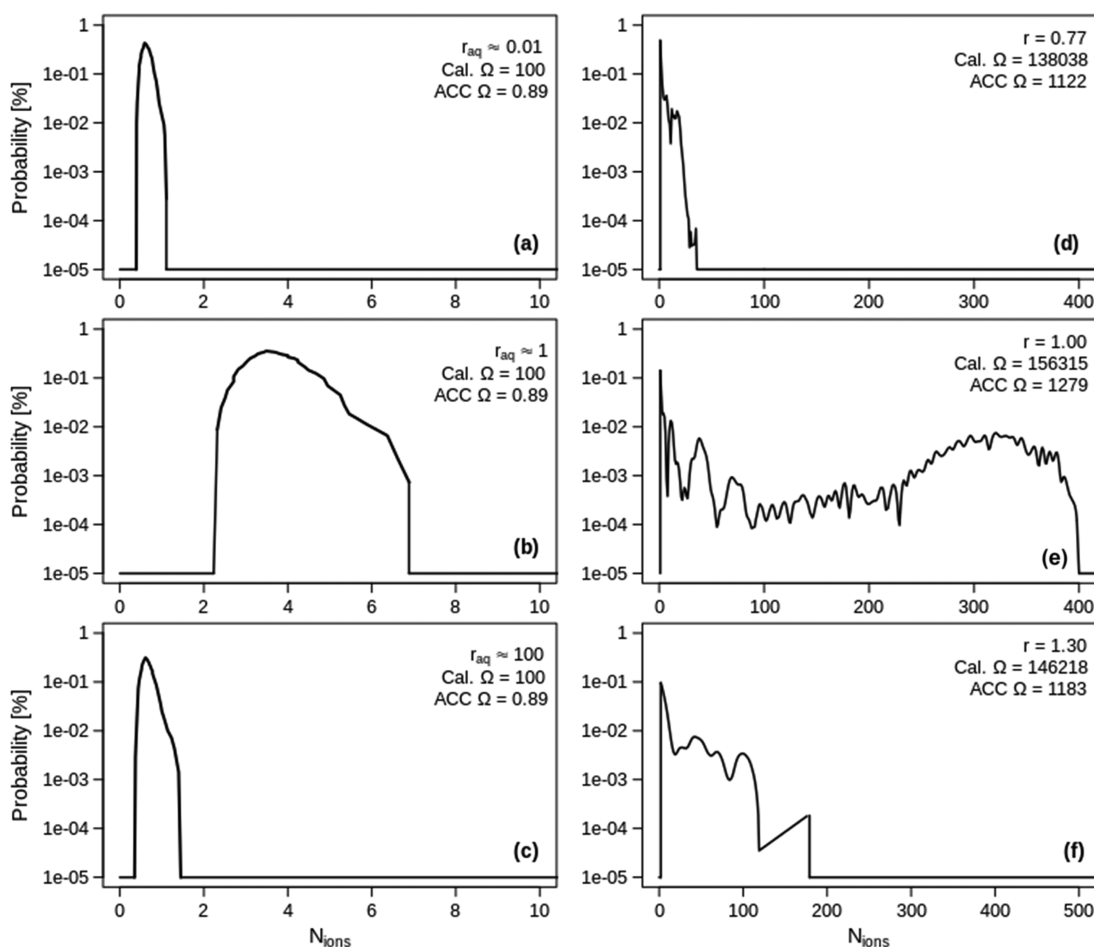
Figure 4. Probability (log-scale) of an aggregate of certain size (consisting of a number of ions) at different initial stoichiometric conditions. The images in (a–c) are based on DLS experiments and contained an initial Ω_{cal} of 100, while (d–f) are based on MD simulations, with $\Omega_{cal} \sim$ 138 000−157 000.

big particle, but with variable stoichiometry. Figure S10b displays the normalized energy for the systems starting with fully solvated ions. In both cases, the normalized energies are larger than 1, indicating that the particles are stable over the entire simulation time (eq 3). Ideally, the normalized energies for the systems starting with fully solvated ions should be unity at 0 ns of simulation time. However, due to the system's setup, e.g., high concentrations, cell size constraints, and the force field, the solvated ions form ion pairs and small particles within less than 1 ps. Consequently, the normalized energies are >1.4 (nearly) instantaneously. The normalized energies in Figure S10a are slightly lower than those in Figure S10b, most likely because the large particles were created in vacuum and at high temperatures before cooling down and added into water.[70] Nevertheless, all particles generated/observed in the MD simulations are energetically stable, irrespective of their stoichiometries.

All particles formed in the simulations showed some rearrangement by shedding ions (i.e., ions going back into bulk solution). The (most extremely) nonstoichiometric particles shed most of the excess ions during the first nanosecond of simulation time to create a more stable particle. For example, the system where the surface of the particle started with a stoichiometry of 4.85 shed 39 calcium atoms after 1 ns and continued to shed less extensively during the remainder of the simulation, thereby creating a stable particle

that is nearly stoichiometric at the surface. The same trend was observed (i.e., release of CO_3 in similar amounts) for the system starting with a stoichiometry of 0.77 at the surface of the particle. The system starting with a particle that was stoichiometric at the surface released excess atoms more gradually (Figure S11 in Section SXI, SI).

Also, the stoichiometry slightly changed for the systems starting from fully solvated ions. After 20 ns, the stoichiometric system changed to a stoichiometry of 1.42, the one starting from 0.77 changed to 0.37, and the one with a starting stoichiometry of 1.30 evolved to 2.76 (Figure S12 in Section SXII, SI).

Direct comparison between DLS and MD results for the impact of stoichiometry was facilitated by the conversion into probability curves as a function of particle size (Figure 4). The curves in Figure 4a−c display the probabilities of the initial DLS measurement, while in Figure 4d−f, the MD simulations are displayed. For both DLS and MD, it is more likely to find larger particles in stoichiometric solutions (Figure 4b,e), compared to the solutions where the stoichiometry deviated from one. Note that overall larger particles were observed in the simulated stoichiometric solution because of the much higher Ω than for the DLS measurements.

From the probability curves, it is clear that there is a slightly higher chance of finding larger particles in $r_{aq} > 1$ than in $r_{aq} < 1$. The probability curves at $r_{aq} > 1$ are broader, i.e., extending
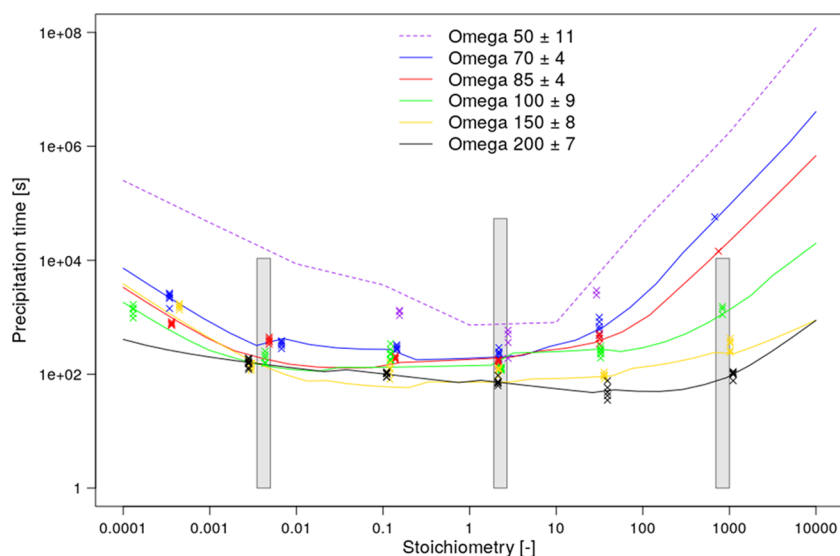
Figure 5. Behavior of eq 4 with stoichiometry and omega. The gray bars show the timescale of our DLS experiments. The fitting does not show smooth curves because the pH is slightly different for the various solutions used in the experiments.

to larger particle sizes, in particular for the MD results (Figure 4d versus f). These observations imply that the particle formation is favored under Ca^{2+}-excess conditions compared to the particle formation in CO_3^{2-} excess solutions. The reason why Ca^{2+}-excess solutions tend to form larger particles more quickly than Ca^{2+}-limiting solutions may be explained by the difference in coordination number between Ca^{2+} and CO_3^{2-}. Demichelis et al.[28] and Smeets et al.[31] found that CO_3^{2-} binds more Ca^{2+} than vice versa. It implies that, in solutions where Ca^{2+} is in excess, larger particles are formed and they form faster, just as we observed here.

3.4. Precipitation Time Measurements. While MD and DLS showed the first steps of the (pre-)nucleation and growth mechanisms involved in $CaCO_3$ formation, XPL was used to gain insight into the larger time and length scales of $CaCO_3$ formation. With this technique, the recorded precipitation time represents the nucleation and growth up to approximately 20 μm $CaCO_3$ crystals.

Generally, four main trends were observed (Figure S4.3 and crosses in Figure 5). First, precipitation times generally decreased with increasing supersaturation with respect to $CaCO_3$. This is in agreement with many previous studies[11,29,47,48,98,99] and general nucleation theory.[79,100] Second, $CaCO_3$ precipitation time was shortest at a given Ω whenever $r_{aq} \sim 1$. This shows that $CaCO_3$ crystal formation is favored around $r_{aq} = 1$, when the two constitutive ions initially have equal activities. Third, the precipitation time in relation to solution stoichiometry shows an asymmetric behavior. Crystals needed significantly more time to form whenever CO_3^{2-} became limiting compared to Ca^{2+}-limiting conditions and is in agreement with our DLS (Figure 4a versus c) and MD (Figure 4d versus f) observations as well as previous findings.[28,31] This asymmetric behavior was less pronounced with increasing Ω and diminished at $\Omega_{cal} \geq 150$. For example, at $\Omega_{cal} = 200$, the precipitation time is only 10-fold longer at $r_{aq} \sim 0.0001$ compared to $r_{aq} \sim 1$, while at $\Omega_{cal} = 70$, the difference is more pronounced as the precipitation time is approximately a 100 times longer. The trends here will be discussed further, in combination with the DLS and MD observations, in Section 3.5.

The variation in precipitation time ($t_{precipitation}$) with r_{aq} and Ω_{cal} that was observed in the XPL experiments can be described by an empirical relationship. The empirical relationship that describes the $CaCO_3$ precipitation time ($t_{precipitation}$) as a function of r_{aq}, Ω_{cal}, pH, and I based on our observed data is

$$
\begin{aligned}
& t_{precipitation}(r_{aq},\ \Omega_{cal},\ pH,\ I,\ a,\ b,\ c,\ d,\ e,\ f) \\
& = \left(\frac{r_{aq}^a + b}{r_{aq} \times 1.2b} + r_{aq}^c \right) \times (\sqrt{\Omega_{cal}} - 1)^d \times pH^e \times I^{-1} \\
& \quad \times f
\end{aligned} \tag{4}
$$

where "a", "b", and "c" are empirically estimated parameters, and "d", "e", and "f" are constants derived from previously conducted research[20,93,94] (see the detailed discussion in Section SIV, SI). Figure 5 shows that the reduction of the empirical equation to its final state is justified and that eq 4 describes our observations well.

3.5. Impact of Stoichiometry on Precipitation Time. The shorter precipitation times observed at $r_{aq} \sim 1$ may be caused by several processes. First of all, calcite growth kinetics through ion-by-ion attachment is fastest near $r_{aq} = 1$.[17,20,21,23] Therefore, once formed, the $CaCO_3$ crystals can grow fastest to reach the size range visible in XPL from solutions with $r_{aq} = 1$. However, this dependency of growth kinetics on r_{aq} becomes stronger at higher Ω values,[102] while here the opposite is observed (Figure 5). The decreased dependence of precipitation time on r_{aq} toward higher Ω therefore suggests that the trends observed here are caused by more factors than just growth kinetics. Besides ion-by-ion attachment, $CaCO_3$-ion pairs and larger aqueous clusters are also known to play a role during the formation of ACC[25,26,31,82,103−106] and during calcite growth.[22,107] While in principle the $CaCO_3$-ion-pair concentration is considered constant at constant Ω, due to its constant relationship with regard to the ion activity product,[21] this consideration only holds under chemostat conditions, such as flow-through systems. In the current batch-type experiments at $r_{aq} = 1$, this consideration may still be valid, but in solutions with $r_{aq} \neq 1$, as soon as nanoparticles formation starts, Ω drops

and nonstoichiometry increases in solution (see limitation Section 3.6). As a result, it is quite likely that the chance of ion-pair formation and the ion-pair activity decreases more strongly than Ω would suggest, although it would require a statistical approach such as that of Hellevang et al.[22] to demonstrate this. This effect may be most pronounced at a lower initial Ω, when the initial ion-pair activity is lower, potentially explaining why the dependence of precipitation time on r_{aq} decreases toward higher Ω.

Aggregation of $CaCO_3$ nanoparticles was clearly observed with the DLS (Figure S7 in Section SVII, SI) and occurred on the same timescale as the precipitation times observed with XPL (gray bars in Figure 5). In particular, for $\Omega_{cal} = 150$ and 200, the gaps in size distribution indicate aggregation, although we cannot rule out that (multiple steps of) aggregation occurred in the $\Omega_{cal} = 100$ experiments. Potentially, this pathway is less dependent on r_{aq} or becomes less dependent on solution stoichiometry at higher Ω_{cal} values. This may be the case when particle charging is also considered.

The calcite surface is known to adsorb excess Ca^{2+} or excess CO_3^{2-}, as shown by changes in its ζ potential.[108−110] It may be assumed that the particles formed in the current experiments at $r_{aq} \neq 1$ also adsorbed the excess ion, leading to the buildup of surface charge.

Moreover, aggregation of uncharged particles will be more favorable compared to charged particles, where higher charges may lead to behavior like charge-stabilized colloids.[111−113] Potentially, such behavior was observed here (Figure 4), where particles predominantly remained below 10 nm at $r_{aq} \neq 1$. Further investigations of particle charging behavior is needed to confirm or rule out this hypothesis, but it can be envisaged that, when at increasing Ω more smaller particles form and/or dense liquid separation occurs,[114−116] the influence of nonstoichiometry on particle surface charge decreases. With more smaller particles, the total surface area will be higher, yielding a lower charge density per particle at the same value for r_{aq}. As a result, for increasing Ω, the influence of nonstoichiometry on the precipitation behavior becomes apparent only at increasingly extreme values of r_{aq}. This is observed in the precipitation time experiments (Figure 5).

A final process that may have affected the observed precipitation times is related to the tendency of the amorphous nanoparticles to reorder structurally. In the MD simulations that started from ~2 nm amorphous particles ($\Omega_{cal} \sim 156\,000$; pH $\geq$ 10.5), it was observed that nonstoichiometric particles tend to lose ions, readjust their size, and attempt to reach electroneutrality. Meanwhile, the stoichiometric particle does not experience much dissolution and the size variations during the simulation time is not as notable as the initially charged particles. Therefore, they may be more ready to aggregate further with other particles or continue growing by gaining smaller entities. This also supports the notion that fastest nucleation occurs in stoichiometric systems.

3.6. Limitations. A typical limitation of batch experiments is that the solution chemistry changes substantially. This also holds for the stoichiometry after the first precipitate forms.[117] Therefore, it is unlikely that constant precipitation kinetics persist throughout our batch precipitation experiments. According to Genovese et al.,[118] the stoichiometry of Ca^{2+}/CO_3^{2-} shifts from 1 to around 100 after a few hours. Yet, their nucleation experiments were performed at lower pH (pH $\sim$ 7), where the bulk solution becomes much more CO_3^{2-}-limiting as the precipitation proceeds compared to pH $\geq$ 10.5. In

addition, they showed that the activity of $CaHCO_3^+$, which acts as a source to provide more growth units, at lower pH during $CaCO_3$ nucleation is much more significant, but Demichelis et al.[28] showed that at a high pH, as used in our experiments, the activity of $CaHCO_3^+$ is negligible. The latter study showed that at pH $\geq$ 10.5, the activity of any calcium hydroxides is limited. We performed, therefore, calculations in PHREEQC[119] (using phreeqc.dat and assuming standard precipitation kinetics from Plummer et al.[120]) to estimate the stoichiometry shift during the precipitation. We noted that, for example, at initial $\Omega_{cal} = 200$ and $r_{aq} \sim 0.001$ (one of the more extreme cases), the stoichiometry shifted to ~0.00001 (so approximately by 2 orders of magnitude). The same magnitude of shift was seen at initial $r_{aq} \sim 1000$. For the stoichiometric solution at $\Omega_{cal} = 200$, the final stoichiometry differed negligibly from the initial one.

One important limitation of the measured particle size by DLS is related to the assumption of spherical particles. This may be oversimplified, depending on which polymorph is forming. In addition, we ignored the fact that small and disordered particles may have a different refractive index than a larger crystal phase in the same solution. For example, crystalline quartz (SiO_2) has a refractive index of 1.552−1.554 at a wavelength of 632 nm,[121] while amorphous SiO_2 (pure quartz glass) has a refractive index of 1.458 at the same wavelength.[122,123] It is therefore likely that the refractive index (RI) of our $CaCO_3$ evolved over the course of the experiments, toward the value for calcite (1.65). For a more realistic comparison of particle size distributions among different chemical conditions, the translational diffusion coefficient is a more accurate quantity. Yet, we were more interested in the trend of relative size distribution development in time, rather than the absolute sizes of the particles. If we can assume a similar decrease of 0.1 for the RI of amorphous $CaCO_3$ compared to calcite then, for example, a $CaCO_3$ particle with a measured size of 825 nm and an RI of 1.59 (calcite) shifts to approximately 712 nm when the RI is changed to 1.49. This shift in apparent size becomes smaller with decreasing particle size.

The size distribution between 100 and 2000 nm was regarded as precipitate-sized materials as the prenucleation particles obtained the critical size[79,101,124,125] to form a crystal structure and nucleate. In addition, the size became large enough for the crystals to sink to the bottom of the cuvette during the experiment. Consequently, the number of precipitate-sized particles may be underestimated, especially with time (i.e., sedimentation of particles increases with particle growth). Possible dust-sized particles were assumed to be of cemental origin, which typically are as small as 2000 nm. Dust particles have a density much smaller than $CaCO_3$ and, consequently, can float in solution while particle size measurements were being performed. For example, Figure 1 shows that some dust particles were measured after 30 min, whose sizes were >2000 nm. However, also note that crystalline particles of similar size were observed in similar time frames under similar experimental conditions using XPL. Still, in the case of the DLS experiments, we cannot rule out potential contributions of dust particles since the precipitates have a much higher density (2.71 g cm^{-3}) for calcite versus 0.51 g cm^{-3} (bulk) for cemental dust[126] and would more likely accumulate on the bottom of the cuvette. Such large precipitates might have been measured coincidentally once

or twice in one or two subrun(s) of the measurement, but not in all 20 subruns that one measurement contained.

Another limitation of the DLS method applied here is that numbers (%) were compared. This means that relative differences are determined, rather than absolute. As a result, some of the decreases in size observed here may actually be caused by larger particles growing beyond detectable size and/ or settling. When these large particles do not contribute to the scattered light, the percent of smaller particles increases.

Finally, the challenge in this type of DLS measurements, especially in the chosen initial Ω and r_{aq}, is the stochastic nature of nucleation events and that DLS measurements are sensitive to several parameters, including density, refractive index variations, and contributions of scattering by water (Section SXIII, SI). We have taken the utmost care to avoid artificial density variations due to the presence of dust particles and air bubbles, but density variations can be expected in our system, where potentially dense liquids[116] and dehydration of precursor phases[95] can occur during the (trans)formation of calcium carbonate crystals. Arguably, some of the variability in particle size with time may be explained by such sensitivity and stochasticity. Nevertheless, the systematic variation in particle size evolution with time for different r_{aq} values, as well as the fact that there is agreement with the trends observed in simulations and XPL, strongly suggests that the observed trends are at least in part due to sensitivity of calcium carbonate formation to solution stoichiometry.

When comparing the DLS results with the XPL results, it is important to keep in mind that the DLS results were obtained in polystyrene cuvettes, while the XPL experiments were conducted in glass. The reactor/vessel material is known to affect the timing of 3D nucleation due to differences in wettability and surface structure.[127]

As mentioned above, it is important to consider the nature of precipitation time determined by XPL. During the measurements, the crystals became visible when the crystal size was about 20 μm (see Section SII (SI) for how this size was determined). Such dimensions imply that a newly formed crystal has already gone through the process of crystal growth extensively and the time registered is not a pure nucleation "induction" time.[100] For that reason, we use the term "precipitation time" rather than the induction time, especially since different crystal growth rates exist at different Ω_{cal} and r_{aq} values. We therefore used this method to investigate the effect of Ω and r_{aq} on the time needed for nucleation and subsequent growth to a 20 μm crystal, a relevant range for many industrial and engineering systems.

3.7. Implications. According to classical nucleation theory (CNT), induction time and nucleation rate depend on the degree of supersaturation and available surface area.[67,79,128,129] In our experiments and simulations, the initial degree of supersaturation with respect to calcite was kept constant, while the solution stoichiometry varied over several orders of magnitude, and a strong variation in timing (Figure 5) and size (Figures 4 and S8) during CaCO$_3$ precipitation was observed. Potentially, these results imply that induction time and nucleation rate depend on r_{aq}, just like the growth rate.[15,16,18−22] A similar observation was recently reported by Legg et al.,[130] who measured different induction times and nucleation rates of iron oxyhydroxide nanoparticle formation at varying pH (essentially varying Fe/OH$^-$). CNT currently fails to explain these observations. This implies that we may need to extend this theory for electrolyte crystals such as CaCO$_3$ and include solution stoichiometry.

The results presented here show that, when solution stoichiometry is varied, precipitation of CaCO$_3$ may occur much more rapidly, reaching 20 μm crystals within minutes versus (more than) days. So, besides increasing/decreasing the degree of supersaturation and/or using additives, adjusting the solution stoichiometry is proposed as an additional, impurity-free method to tailor CaCO$_3$ crystallization processes. Solution stoichiometry can also be altered by adjusting the pH, apart from the concentrations of the respective ions, as it directly affects the activity of CO$_3{}^{2-}$, besides Ω. Ultimately, the desired timescale for CaCO$_3$ crystallization may be coordinated.

4. CONCLUSIONS

Our experimental and computational results show that the {Ca^{2+}}:{CO$_3{}^{2-}$} in the solution has a strong impact on the pathway and timing of CaCO$_3$ nucleation and growth. At the same initial degree of supersaturation, CaCO$_3$ precipitation

- is typically fastest when {Ca^{2+}} = {CO$_3{}^{2-}$};
- is slower in excess Ca^{2+} solutions compared to solutions with a similar excess in CO$_3{}^{2-}$, especially at lower Ω;
- occurs through aggregation of prenucleation clusters at high Ω; and
- time is less dependent on r_{aq} at higher Ω.

The dependence of CaCO$_3$ precipitation time on solution stoichiometry at different degrees of supersaturation can be described with an empirical rate law, which can be used to better predict CaCO$_3$ formation and to tailor or improve industrial CaCO$_3$ precipitation processes.

■ ASSOCIATED CONTENT

ⓢ Supporting Information

The Supporting Information is available free of charge at https://pubs.acs.org/doi/10.1021/acs.cgd.0c01403.

> Sketch of XPL experimental setup (Section SI); explanation of CaCO$_3$ behavior in XPL (Section SII); XPL experimental definition for precipitation time (Section SIII); details on obtained fitting equation (Sections SIV and SV); more detailed DLS results (Sections SVI−SIX); simulation details (Sections SX−SXII); and comparison between UPW and CaCO$_3$ DLS measurements (Section SXIII) (PDF)

■ AUTHOR INFORMATION

Corresponding Author

    Sergěj Y. M. H. Seepma − *Department of Earth Sciences, Utrecht University, 3584 CB Utrecht, The Netherlands;* ⓘ orcid.org/0000-0002-9033-8528; Email: s.y.m.h.seepma@uu.nl

Authors

    Sergio E. Ruiz-Hernandez − *Department of Earth Sciences, Utrecht University, 3584 CB Utrecht, The Netherlands;* ⓘ orcid.org/0000-0003-3149-7331

    Gernot Nehrke − *Alfred-Wegener Institut: Helmholtz-Zentrum für Polar- und Meeresforschung, 27570 Bremerhaven, Germany*

    Karline Soetaert − *Department of Earth Sciences, Utrecht University, 3584 CB Utrecht, The Netherlands; Estuarine & Delta Systems Department, NIOZ: Royal Netherlands*

Institute for Sea Research, 4401 NT Yerseke, The Netherlands

Albert P. Philipse − *Van't Hoff Laboratory for Physical and Colloid Chemistry, Debye Institute for Nanomaterials Science, Utrecht University, 3584 CH Utrecht, The Netherlands*

Bonny W. M. Kuipers − *Van't Hoff Laboratory for Physical and Colloid Chemistry, Debye Institute for Nanomaterials Science, Utrecht University, 3584 CH Utrecht, The Netherlands*

Mariette Wolthers − *Department of Earth Sciences, Utrecht University, 3584 CB Utrecht, The Netherlands;* orcid.org/0000-0003-3908-5622

Complete contact information is available at:
https://pubs.acs.org/10.1021/acs.cgd.0c01403

Notes
The authors declare no competing financial interest.

■ REFERENCES

(1) Davila, V. G.; Dominguez, E. J. S. Stabilized Pipe Scaling Remover and Inhibitor Compound. US9,085,748B2, 2015.

(2) Gunther, D. A. Process for Preventing the Formation of Boiler Scale. US3,308,062A, 1967.

(3) Zhang, J.; Wang, Q.; Jiang, J. Lime mud from paper-making process addition to food waste synergistically enhances hydrogen fermentation performance. *Int. J. Hydrogen Energy* **2013**, *38*, 2738−2745.

(4) Doberšek, D.; Goričanec, D. Influence of water scale on thermal flow losses of domestic appliances. *Int. J. Math. Models Methods Appl. Sci.* **2007**, *1*, 55−61.

(5) Kermani, M. B.; Harrop, D. The impact of corrosion on oil and gas industry. *SPE Prod. Facil.* **1996**, *11*, 186−190.

(6) Birnhack, L.; Voutchkov, N.; Lahav, O. Fundamental chemistry and engineering aspects of post-treatment processes for desalinated water—a review. *Desalination* **2011**, *273*, 6−22.

(7) Huber, P. Kinetics of CO_2 Stripping and Its Effect on the Saturation State of $CaCO_3$ upon Aeration of a $CaCO_3$−CO_2−H_2O System: Application to Scaling in the Papermaking Process. *Ind. Eng. Chem. Res.* **2011**, *50*, 13655−13661.

(8) School of Ocean and Earth Sciences and Technology Hawaii (SOEST). Chemical Composition of Sawater: Salinity and the Major Constituents, 2017. http://www.soest.hawaii.edu/oceanography/courses/OCN623/Spring2018/5-Salinity2018.pdf.

(9) Los Angeles Department of Water and Power (LADWP). Mono Lake Mineral Water Quality. http://www.monobasinresearch.org/images/mbeir/dchapter3/table3b-2.pdf.

(10) Waternet Lims Database. Water Quality Data at Drinking Water Production Plant Weesperkarspel (Feb 28, 2018).

(11) Morse, J. W.; Arvidson, R. S.; Lüttge, A. Calcium carbonate formation and dissolution. *Chem. Rev.* **2007**, *107*, 342−381.

(12) Meldrum, F. C.; Cölfen, H. Controlling mineral morphologies and structures in biological and synthetic systems. *Chem. Rev.* **2008**, *108*, 4332−4432.

(13) Declet, A.; Reyes, E.; Suárez, O. M. Calcium carbonate precipitation: A review of the carbonate crystallization process and application in bioinspired composites. *Rev. Adv. Mater. Sci.* **2016**, *44*, 87−107.

(14) Chang, R.; Kim, S.; Lee, S.; Choi, S.; Kim, M.; Park, Y. Calcium carbonate precipitation for CO_2 storage and utilization: a review of the carbonate crystallization and polymorphism. *Front. Energy Res.* **2017**, *5*, No. 17.

(15) Paquette, J.; Reeder, R. J. Relationship between surface structure, growth mechanism, and trace element incorporation in calcite. *Geochim. Cosmochim. Acta* **1995**, *59*, 735−749.

(16) Tai, C. Y.; Chang, M. C.; Wu, C. K.; Lin, Y. C. Interpretation of calcite growth data using the two-step crystal growth model. *Chem. Eng. Sci.* **2006**, *61*, 5346−5354.

(17) Nehrke, G. Calcite Precipitation from Aqueous Solution: Transformation from Vaterite and Role of Solution Stoichiometry. Doctoral Dissertation, Utrecht University Department of Earth Sciences, 2007.

(18) Tribello, G. A.; Bruneval, F.; Liew, C.; Parrinello, M. A molecular dynamics study of the early stages of calcium carbonate growth. *J. Phys. Chem. B* **2009**, *113*, 11680−11687.

(19) Larsen, K.; Bechgaard, K.; Stipp, S. L. S. The effect of the Ca^{2+} to $CO_3^{2−}$ activity ratio on spiral growth at the calcite {1014} surface. *Geochim. Cosmochim. Acta* **2010**, *74*, 2099−2109.

(20) Stack, A. G.; Grantham, M. C. Growth rate of calcite steps as a function of aqueous calcium-to-carbonate ratio: independent attachment and detachment of calcium and carbonate ions. *Cryst. Growth Des.* **2010**, *10*, 1409−1413.

(21) Wolthers, M.; Van der Gaast, S. J.; Rickard, D. The structure of disordered mackinawite. *Am. Mineral.* **2003**, *88*, 2007−2015.

(22) Hellevang, H.; Haile, B. G.; Miri, R. A Statistical Approach To Explain the Solution Stoichiometry Effect on Crystal Growth Rates. *Cryst. Growth Des.* **2016**, *16*, 1337−1348.

(23) Sand, K. K.; Tobler, D. J.; Dobberschütz, S.; Larsen, K. K.; Makovicky, E.; Andersson, M. P.; Wolthers, M.; Stipp, S. L. S. Calcite Growth Kinetics: Dependence on Saturation Index, Ca^{2+}: $CO_3^{2−}$ Activity Ratio, and Surface Atomic Structure. *Cryst. Growth Des.* **2016**, *16*, 3602−3612.

(24) Wang, Y. W.; Kim, Y. Y.; Stephens, C. J.; Meldrum, F. C.; Christenson, H. K. In situ study of the precipitation and crystallization of amorphous calcium carbonate (ACC). *Cryst. Growth Des.* **2012**, *12*, 1212−1217.

(25) Gebauer, D.; Völkel, A.; Cölfen, H. Stable prenucleation calcium carbonate clusters. *Science* **2008**, *322*, 1819−1822.

(26) Gebauer, D.; Cölfen, H. Prenucleation clusters and nonclassical nucleation. *Nano Today* **2011**, *6*, 564−584.

(27) Rodriguez-Blanco, J. D.; Shaw, S.; Benning, L. G. The kinetics and mechanisms of amorphous calcium carbonate (ACC) crystallization to calcite, via vaterite. *Nanoscale* **2011**, *3*, 265−271.

(28) Demichelis, R.; Raiteri, P.; Gale, J. D.; Quigley, D.; Gebauer, D. Stable prenucleation mineral clusters are liquid-like ionic polymers. *Nat. Commun.* **2011**, *2*, No. 590.

(29) Bots, P.; Benning, L. G.; Rodriguez-Blanco, J. D.; Roncal-Herrero, T.; Shaw, S. Mechanistic insights into the crystallization of amorphous calcium carbonate (ACC). *Cryst. Growth Des.* **2012**, *12*, 3806−3814.

(30) Nielsen, M. H. In Situ Investigations into $CaCO_3$ Nucleation. Doctoral Dissertation, UC Berkeley, 2015.

(31) Smeets, P. J.; Finney, A. R.; Habraken, W. J.; Nudelman, F.; Friedrich, H.; Laven, J.; De Yoreo, J. J.; Rodger, P. M.; Sommerdijk, N. A. A classical view on nonclassical nucleation. *Proc. Natl. Acad. Sci. U.S.A.* **2017**, *114*, E7882−E7890.

(32) Chaka, A. M.; Felmy, A. R.; Qafoku, O. Ab initio thermodynamics of magnesium carbonates and hydrates in water-saturated supercritical CO_2 and CO_2-rich regions. *Chem. Geol.* **2016**, *434*, 1−11.

(33) Zou, Z.; Habraken, W. J.; Bertinetti, L.; Politi, Y.; Gal, A.; Weiner, S.; Fratzl, P.; Addadi, L. On the phase diagram of calcium carbonate solutions. *Adv. Mater. Interfaces* **2017**, *4*, No. 1600076.

(34) Chaka, A. M. Ab initio thermodynamics of hydrated calcium carbonates and calcium analogues of magnesium carbonates: implications for carbonate crystallization pathways. *ACS Earth Space Chem.* **2018**, *2*, 210−224.

(35) Avaro, J. T.; Wolf, S. L.; Hauser, K.; Gebauer, D. Stable Prenucleation Calcium Carbonate Clusters Define Liquid−Liquid Phase Separation. *Angew. Chem., Int. Ed.* **2020**, *59*, 6155−6159.

(36) Mergelsberg, S. T.; De Yoreo, J. J.; Miller, Q. R.; Michel, F. M.; Ulrich, R. N.; Dove, P. M. Metastable solubility and local structure of amorphous calcium carbonate (ACC). *Geochim. Cosmochim. Acta* **2020**, *289*, 196−206.

(37) Takasaki, S.; Parsiegla, K. I.; Katz, J. L. Calcite growth and the inhibiting effect of iron (III). *J. Cryst. Growth* **1994**, *143*, 261−268.

(38) Loste, E.; Wilson, R. M.; Seshadri, R.; Meldrum, F. C. The role of magnesium in stabilising amorphous calcium carbonate and controlling calcite morphologies. *J. Cryst. Growth* **2003**, *254*, 206−218.

(39) Lin, Y. P.; Singer, P. C. Inhibition of calcite crystal growth by polyphosphates. *Water Res.* **2005**, *39*, 4835−4843.

(40) Lin, Y. P.; Singer, P. C.; Aiken, G. R. Inhibition of calcite precipitation by natural organic material: kinetics, mechanism, and thermodynamics. *Environ. Sci. Technol.* **2005**, *39*, 6420−6428.

(41) Lin, Y. P.; Singer, P. C. Effect of Mg^{2+} on the kinetics of calcite crystal growth. *J. Cryst. Growth* **2009**, *312*, 136−140.

(42) Vavouraki, A. I.; Putnis, C. V.; Putnis, A.; Koutsoukos, P. G. An Atomic Force Microscopy study of the growth of calcite in the presence of sodium sulfate. *Chem. Geol.* **2008**, *253*, 243−251.

(43) Radha, A. V.; Forbes, T. Z.; Killian, C. E.; Gilbert, P. U. P. A.; Navrotsky, A. Transformation and crystallization energetics of synthetic and biogenic amorphous calcium carbonate. *Proc. Natl. Acad. Sci. U.S.A.* **2010**, *107*, 16438−16443.

(44) Reddy, M. M. Calcite growth-rate inhibition by fulvic acid and magnesium ion—Possible influence on biogenic calcite formation. *J. Cryst. Growth* **2012**, *352*, 151−154.

(45) Rodriguez-Navarro, C.; Benning, L. G. Control of crystal nucleation and growth by additives. *Elements* **2013**, *9*, 203−209.

(46) Radha, A. V.; Navrotsky, A. Direct experimental measurement of water interaction energetics in amorphous carbonates MCO_3 (M= Ca, Mn, and Mg) and implications for carbonate crystal growth. *Cryst. Growth Des.* **2015**, *15*, 70−78.

(47) He, S.; Kan, A. T.; Tomson, M. B. Inhibition of calcium carbonate precipitation in NaCl brines from 25 to 90 °C. *Appl. Geochem.* **1999**, *14*, 17−25.

(48) Stamatakis, E.; Stubos, A.; Palyvos, J.; Chatzichristos, C.; Muller, J. An improved predictive correlation for the induction time of $CaCO_3$ scale formation during flow in porous media. *J. Colloid Interface Sci.* **2005**, *286*, 7−13.

(49) Gustafsson, J. P. *Visual Minteq v3.1, a free equilibrium speciation model*; KTH, Department of Land and Water Resources Engineering: Stockholm, Sweden, 2013. http://vminteq.lwr.kth.se/.

(50) Plummer, L. N.; Busenberg, E. The solubilities of calcite, aragonite and vaterite in CO_2-H_2O solutions between 0 and 90 °C, and an evaluation of the aqueous model for the system $CaCO_3$-CO_2-H_2O. *Geochim. Cosmochim. Acta* **1982**, *46*, 1011−1040.

(51) Davies, C. W. *Ion Association*; Butterworths, 1962.

(52) Malvern Instruments Ltd. *Zetasizer Nano Series User Manual*, MAN0317, issue 1.1; Malvern Instruments Ltd., 2004.

(53) Malvern Instruments Ltd. *Dynamic Light Scattering: An Introduction in 30 Minutes*, Technical Note Malvern, MRK656-01; Malvern Instruments Ltd., 2012; pp 1−8.

(54) Babick, F. *Suspensions of Colloidal Particles and Aggregates*; Springer: Cham, Switzerland, 2016.

(55) Wiese, H.; Horn, D. Single-mode fibers in fiber-optic quasielastic light scattering: A study of the dynamics of concentrated latex dispersions. *J. Chem. Phys.* **1991**, *94*, 6429−6443.

(56) Peters, R.; Georgalis, Y.; Saenger, W. Accessing lysozyme nucleation with a novel dynamic light scattering detector. *Acta Crystallogr., Sect. D: Biol. Crystallogr.* **1998**, *54*, 873−877.

(57) Barnett, C. E. Some Applications of Wave-length Turbidimetry in the Infrared. *J. Phys. Chem.* **1942**, *46*, 69−75.

(58) Sutherland, W. LXXV. A dynamical theory of diffusion for non-electrolytes and the molecular mass of albumin. *London, Edinburgh, Dublin Philos. Mag. J. Sci.* **1905**, *9*, 781−785.

(59) Born, M.; Wolf, E. *Principles of Optics: Electromagnetic Theory of Propagation, Interference and Diffraction of Light*; Oxford Pergamon Press: U.K., 2013.

(60) Brown, W. *Dynamic Light Scattering: The Method and Some Applications*; Oxford Clarendon Press: England, 1993.

(61) Provencher, S. W. A constrained regularization method for inverting data represented by linear algebraic or integral equations. *Comput. Phys. Commun.* **1982**, *27*, 213−227.

(62) Provencher, S. W. CONTIN: a general purpose constrained regularization program for inverting noisy linear algebraic and integral equations. *Comput. Phys. Commun.* **1982**, *27*, 229−242.

(63) Berne, B. J.; Pecora, R. *Dynamic Light Scattering: With Applications to Chemistry, Biology, and Physics*; General Publishing Company Ltd.: Canada, 2000.

(64) Frisken, B. J. Revisiting the method of cumulants for the analysis of dynamic light-scattering data. *Appl. Opt.* **2001**, *40*, 4087−4091.

(65) Shannon, R. D. Revised effective ionic radii and systematic studies of interatomic distances in halides and chalcogenides. *Acta Crystallogr., Sect. A: Cryst. Phys., Diffr., Theor. Gen. Crystallogr.* **1976**, *32*, 751−767.

(66) Jenkins, H. D. B.; Thakur, K. P. Reappraisal of thermochemical radii for complex ions. *J. Chem. Educ.* **1979**, *56*, 576.

(67) Kashchiev, D. *Nucleation*; Elsevier: U.K., 2000.

(68) Sear, R. P. Nucleation: theory and applications to protein solutions and colloidal suspensions. *J. Phys.: Condens. Matter* **2007**, *19*, No. 033101.

(69) Sear, R. P. Quantitative studies of crystal nucleation at constant supersaturation: experimental data and models. *CrystEngComm* **2014**, *16*, 6506−6522.

(70) Raiteri, P.; Gale, J. D. Water is the key to nonclassical nucleation of amorphous calcium carbonate. *J. Am. Chem. Soc.* **2010**, *132*, 17623−17634.

(71) Spagnoli, D.; Cooke, D. J.; Kerisit, S.; Parker, S. C. Molecular dynamics simulations of the interaction between the surfaces of polar solids and aqueous solutions. *J. Mater. Chem.* **2006**, *16*, 1997−2006.

(72) R Core Team. *R: A Language and Environment for Statistical Computing*; R Foundation for Statistical Computing: Vienna, Austria, 2019. https://www.R-project.org/.

(73) Soetaert, K.; Petzoldt, T. Inverse modelling, sensitivity and monte carlo analysis in R using package FME. *J. Stat. Software* **2010**, *33*, 1−28.

(74) Tierney, L.; Mira, A. Some adaptive Monte Carlo methods for Bayesian inference. *Stat. Med.* **1999**, *18*, 2507−2515.

(75) Bédard, M.; Douc, R.; Moulines, E. Scaling analysis of multiple-try MCMC methods. *Stochastic Processes Their Appl.* **2012**, *122*, 758−786.

(76) Soetaert, K.; Hofmann, A. F.; Middelburg, J. J.; Meysman, F. J.; Greenwood, J. Reprint of "The effect of biogeochemical processes on pH". *Mar. Chem.* **2007**, *106*, 380−401.

(77) Egleston, E. S.; Sabine, C. L.; Morel, F. M. Revelle revisited: Buffer factors that quantify the response of ocean chemistry to changes in DIC and alkalinity. *Global Biogeochem. Cycles* **2010**, *24*, No. GB1002.

(78) Hagens, M.; Middelburg, J. J. Generalised expressions for the response of pH to changes in ocean chemistry. *Geochim. Cosmochim. Acta* **2016**, *187*, 334−349.

(79) De Yoreo, J. J.; Vekilov, P. G. Principles of crystal nucleation and growth. *Rev. Mineral. Geochem.* **2003**, *54*, 57−93.

(80) Wolthers, M.; Nehrke, G.; Gustafsson, J. P.; Van Cappellen, P. Calcite growth kinetics: Modeling the effect of solution stoichiometry. *Geochim. Cosmochim. Acta* **2012**, *77*, 121−134.

(81) Michel, F. M.; Antao, S. M.; Chupas, P. J.; Lee, P. L.; Parise, J. B.; Schoonen, M. A. A. Short-to medium-range atomic order and

crystallite size of the initial FeS precipitate from pair distribution function analysis. *Chem. Mater.* **2005**, *17*, 6246−6255.

(82) Gilbert, B.; Ono, R. K.; Ching, K. A.; Kim, C. S. The effects of nanoparticle aggregation processes on aggregate structure and metal uptake. *J. Colloid Interface Sci.* **2009**, *339*, 285−295.

(83) Hu, Q.; Nielsen, M. H.; Freeman, C. L.; Hamm, L. M.; Tao, J.; Lee, J. R. I.; Han, T. Y. J.; et al. The thermodynamics of calcite nucleation at organic interfaces: Classical vs. non-classical pathways. *Faraday Discuss.* **2012**, *159*, 509−523.

(84) Brečević, L.; Nielsen, A. E. Solubility of amorphous calcium carbonate. *J. Cryst. Growth* **1989**, *98*, 504−510.

(85) Blue, C. R.; Rimstidt, J. D.; Dove, P. M. A mixed flow reactor method to synthesize amorphous calcium carbonate under controlled chemical conditions. *Methods Enzymol.* **2013**, *532*, 557−568.

(86) Blue, C. R.; Giuffre, A.; Mergelsberg, S.; Han, N.; De Yoreo, J. J.; Dove, P. M. Chemical and physical controls on the transformation of amorphous calcium carbonate into crystalline $CaCO_3$ polymorphs. *Geochim. Cosmochim. Acta* **2017**, *196*, 179−196.

(87) Kellermeier, M.; Picker, A.; Kempter, A.; Cölfen, H.; Gebauer, D. A straightforward treatment of activity in aqueous CaCO3 solutions and the consequences for nucleation theory. *Adv. Mater.* **2014**, *26*, 752−757.

(88) Clarkson, J. R.; Price, T. J.; Adams, C. J. Role of metastable phases in the spontaneous precipitation of calcium carbonate. *J. Chem. Soc., Faraday Trans.* **1992**, *88*, 243−249.

(89) Lassin, A.; André, L.; Lach, A.; Thadée, A. L.; Cézac, P.; Serin, J. P. Solution properties and salt-solution equilibria in the H-Li-Na-K-Ca-Mg-Cl-H_2O system at 25 °C: A new thermodynamic model based on Pitzer's equations. *Calphad* **2018**, *61*, 126−139.

(90) Steefel, C. I.; Van Cappellen, P. A new kinetic approach to modeling water-rock interaction: The role of nucleation, precursors, and Ostwald ripening. *Geochim. Cosmochim. Acta* **1990**, *54*, 2657−2677.

(91) Mann, S.; Heywood, B. R.; Rajam, S.; Birchall, J. D. Controlled crystallization of $CaCO_3$ under stearic acid monolayers. *Nature* **1988**, *334*, 692−695.

(92) Cölfen, H.; Mann, S. Higher-order organization by mesoscale self-assembly and transformation of hybrid nanostructures. *Angew. Chem., Int. Ed.* **2003**, *42*, 2350−2365.

(93) Ogino, T.; Suzuki, T.; Sawada, K. The formation and transformation mechanism of calcium carbonate in water. *Geochim. Cosmochim. Acta* **1987**, *51*, 2757−2767.

(94) Nudelman, F.; Sonmezler, E.; Bomans, P. H.; de With, G.; Sommerdijk, N. A. Stabilization of amorphous calcium carbonate by controlling its particle size. *Nanoscale* **2010**, *2*, 2436−2439.

(95) Nielsen, M. H.; Aloni, S.; De Yoreo, J. J. In situ TEM imaging of $CaCO_3$ nucleation reveals coexistence of direct and indirect pathways. *Science* **2014**, *345*, 1158−1162.

(96) Bewernitz, M. A.; Gebauer, D.; Long, J.; Cölfen, H.; Gower, L. B. A metastable liquid precursor phase of calcium carbonate and its interactions with polyaspartate. *Faraday Discuss.* **2012**, *159*, 291−312.

(97) Nielsen, M. H.; Li, D.; Zhang, H.; Aloni, S.; Han, T. Y.-J.; Frandsen, C.; Seto, J.; Banfield, J. F.; Cölfen, H.; De Yoreo, J. J. Investigating processes of nanocrystal formation and transformation via liquid cell TEM. *Microsc. Microanal.* **2014**, *20*, 425−436.

(98) Pytkowicz, R. M. Calcium carbonate retention in supersaturated seawater. *Am. J. Sci.* **1973**, *273*, 515−522.

(99) Morse, J. W.; He, S. Influences of T, S and pCO_2 on the pseudo-homogeneous precipitation of $CaCO_3$ from seawater: implications for whiting formation. *Mar. Chem.* **1993**, *41*, 291−297.

(100) Nielsen, A. E. *Kinetics of Precipitation*; Oxford Pergamon Press: U.K., 1964.

(101) Zuddas, P.; Mucci, A. Kinetics of calcite precipitation from seawater: II. The influence of the ionic strength. *Geochim. Cosmochim. Acta* **1998**, *62*, 757−766.

(102) Zhang, J.; Nancollas, G. H. Kink Density and Rate of Step Movement during Growth and Dissolution of an AB-Crystal in a Nonstoichiometric Solution. *J. Colloid Interface Sci.* **1998**, *200*, 131−145.

(103) Gebauer, D.; Kellermeier, M.; Gale, J. D.; Bergström, L.; Cölfen, H. Pre-nucleation clusters as solute precursors in crystallisation. *Chem. Soc. Rev.* **2014**, *43*, 2348−2371.

(104) Pouget, E. M.; Bomans, P. H.; Goos, J. A.; Frederik, P. M.; de With, G.; Sommerdijk, N. A. J. M. The initial stages of template-controlled $CaCO_3$ formation revealed by cryo-TEM. *Science* **2009**, *323*, 1455−1458.

(105) De Yoreo, J. Crystal nucleation: more than one pathway. *Nat. Mater.* **2013**, *12*, 284.

(106) Henzler, K.; Fetisov, E. O.; Galib, M.; Baer, M. D.; Legg, B. A.; Borca, C.; Xto, J. M.; et al. Supersaturated calcium carbonate solutions are classical. *Sci. Adv.* **2018**, *4*, No. eaao6283.

(107) Hellevang, H.; Miri, R.; Haile, B. G. New insights into the mechanisms controlling the rate of crystal growth. *Cryst. Growth Des.* **2014**, *14*, 6451−6458.

(108) Cicerone, D. S.; Regazzoni, A. E.; Blesa, M. A. Electrokinetic properties of the calcite/water interface in the presence of magnesium and organic matter. *J. Colloid Interface Sci.* **1992**, *154*, 423−433.

(109) Wolthers, M.; Charlet, L.; Van Cappellen, P. The surface chemistry of divalent metal carbonate minerals; a critical assessment of surface charge and potential data using the charge distribution multi-site ion complexation model. *Am. J. Sci.* **2008**, *308*, 905−941.

(110) Kasha, A.; Al-Hashim, H.; Abdallah, W.; Taherian, R.; Sauerer, B. Effect of Ca^{2+}, Mg^{2+} and SO_4^{2-} ions on the zeta potential of calcite and dolomite particles aged with stearic acid. *Colloids Surf., A* **2015**, *482*, 290−299.

(111) Ito, K.; Yoshida, H.; Ise, N. Void structure in colloidal dispersions. *Science* **1994**, *263*, 66−68.

(112) Van Roij, R.; Dijkstra, M.; Hansen, J. P. Phase diagram of charge-stabilized colloidal suspensions: van der Waals instability without attractive forces. *Phys. Rev. E* **1999**, *59*, 2010.

(113) Nägele, G.; Heinen, M.; Banchio, A. J.; Contreras-Aburto, C. Electrokinetic and hydrodynamic properties of charged-particles systems. *Eur. Phys. J.: Spec. Top.* **2013**, *222*, 2855−2872.

(114) Faatz, M.; Grohn, F.; Wegner, G. Amorphous calcium carbonate: Synthesis and potential intermediate in biomineralization. *Adv. Mater.* **2004**, *16*, 996−1000.

(115) Cartwright, J. H.; Checa, A. G.; Gale, J. D.; Gebauer, D.; Sainz-Díaz, C. I. Calcium carbonate polyamorphism and its role in biomineralization: how many amorphous calcium carbonates are there? *Angew. Chem., Int. Ed.* **2012**, *51*, 11960−11970.

(116) Wallace, A. F.; Hedges, L. O.; Fernandez-Martinez, A.; Raiteri, P.; Gale, J. D.; Waychunas, G. A.; Whitelam, S.; et al. Microscopic evidence for liquid-liquid separation in supersaturated $CaCO_3$ solutions. *Science* **2013**, *341*, 885−889.

(117) Dai, L.; Douglas, E. P.; Gower, L. B. Compositional analysis of a polymer-induced liquid-precursor (PILP) amorphous $CaCO_3$ phase. *J. Non-Cryst. Solids* **2008**, *354*, 1845−1854.

(118) Genovese, D.; Montalti, M.; Otálora, F.; Gómez-Morales, J.; Sancho-Tomás, M.; Falini, G.; García-Ruiz, J. M. Role of $CaCO_3$ neutral pair in calcium carbonate crystallization. *Cryst. Growth Des.* **2016**, *16*, 4173−4177.

(119) Parkhurst, D. L.; Appelo, C. A. J. *User's Guide to PHREEQC (Version 2): A Computer Program for Speciation, Batch-Reaction, One-Dimensional Transport, and Inverse Geochemical Calculations*, Water-Resources Investigations Report 99-4259; USGS, 1999; p 312.

(120) Plummer, L. N.; Wigley, T. M. L.; Parkhurst, D. L. The kinetics of calcite dissolution in CO_2-water systems at 5 degrees to 60 degrees C and 0.0 to 1.0 atm CO_2. *Am. J. Sci.* **1978**, *278*, 179−216.

(121) Ghosh, G. Dispersion-equation coefficients for the refractive index and birefringence of calcite and quartz crystals. *Opt. Commun.* **1999**, *163*, 95−102.

(122) Malitson, I. H. Interspecimen comparison of the refractive index of fused silica. *J. Opt. Soc. Am.* **1965**, *55*, 1205−1209.

(123) Kitamura, R.; Pilon, L.; Jonasz, M. Optical constants of silica glass from extreme ultraviolet to far infrared at near room temperature. *Appl. Opt.* **2007**, *46*, 8118−8133.

(124) Nielsen, A. E. Nucleation and growth of crystals at high supersaturation. *Krist. Tech.* **1969**, *4*, 17−38.

(125) Abraham, F. F.; Zettlemoyer, A. C. Homogeneous Nucleation Theory. *Phys. Today* **1974**, *27*, 52−53.

(126) Rudzionis, Z.; Ivanauskas, E.; Navickas, A. A. In *Influence of Cement Kiln Dust and Shale Ash on the Cement Stone Properties*, Proceedings of the 10th International Conference on Modern Building Materials, Structures and Techniques, Vilnius Gediminas Technical University, Department of Construction Economics & Property, 2010; p 270.

(127) Xu, W.; Lan, Z.; Peng, B.; Wen, R.; Ma, X. Heterogeneous nucleation capability of conical microstructures for water droplets. *RSC Adv.* **2015**, *5*, 812−818.

(128) Benning, L. G.; Waychunas, G. A. Nucleation, Growth, and Aggregation of Mineral Phases: Mechanisms and Kinetic Controls. In *Kinetics of Water−Rock Interaction*; Brantley, S. L., Kubicki, J. D., White, A. F., Eds.; Springer: NY, 2008; pp 259−333.

(129) Kalikmanov, V. I. Soft depletion in binary fluids. *Phys. Rev. E* **2003**, *68*, No. 010101.

(130) Legg, B. A.; Zhu, M.; Zhang, H.; Waychunas, G.; Gilbert, B.; Banfield, J. F. A model for nucleation when nuclei are non-stoichiometric: Understanding the precipitation of iron oxyhydroxide nanoparticles. *Cryst. Growth Des.* **2016**, *16*, 5726−5737.